Towards high-fidelity modeling of arc-jet environments and material response

ARCHeS
ARC Heater Simulator

DPLR
Data-Parallel Line Relaxation

PATO
Porous-material Analysis Toolbox based on OpenFOAM

Jeremie Meurisse, Sergio Fraile Izquierdo, John Thornton,
Patricia Ventura Diaz, Magnus Haw, Brody Bessire and Nagi Mansour.

Advanced Modeling & Simulation (AMS) Seminar Series
NASA Ames Research Center, September 24th, 2020

Introduction

Arc-Jets

- Arc-jets are essential facilities used in research, development and evaluation of Thermal Protection Systems (TPS) for hypersonic vehicles.
- Arc-jets produce high-enthalpy environments emulating atmospheric planetary entry.
- NASA's facilities:
  - NASA Ames Arc Jet Complex.
  - Hypersonic Materials Environmental Test System (HyMETS).

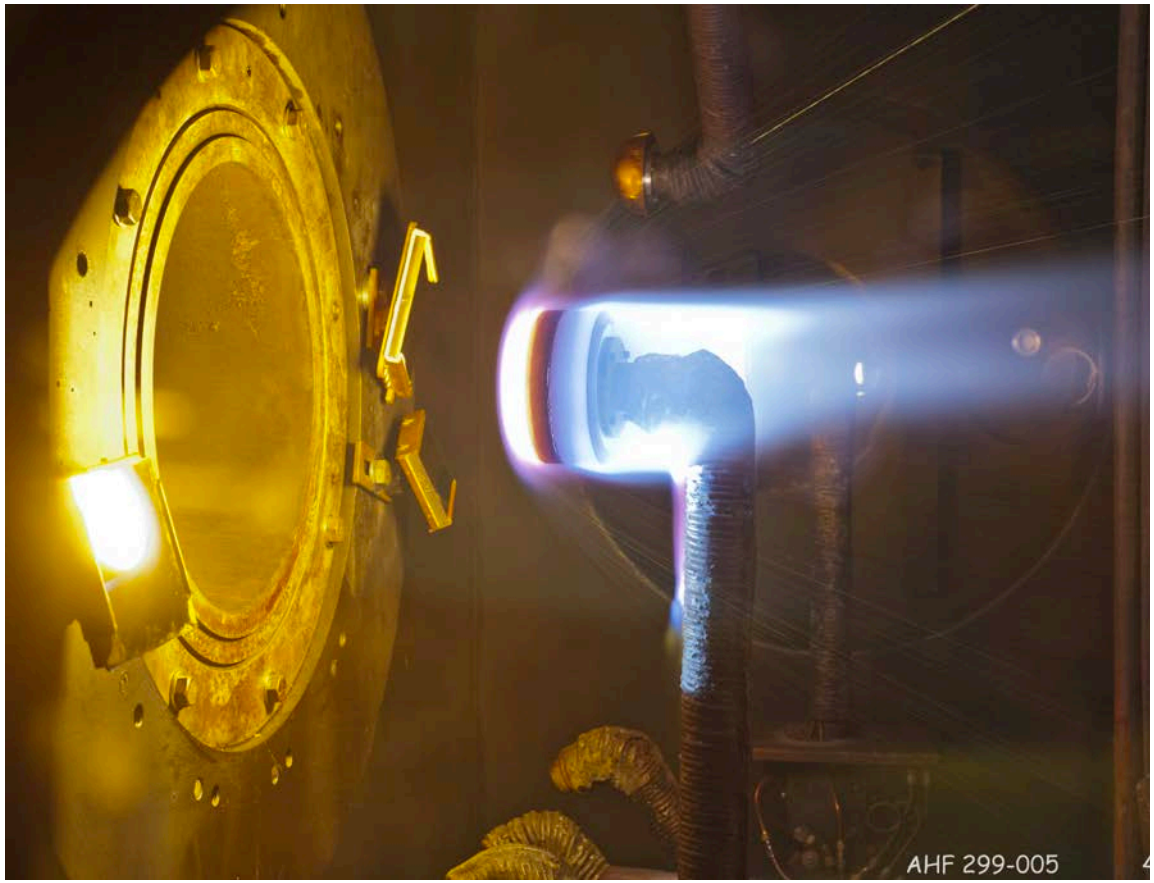

High-fidelity modeling of arc-jet testing

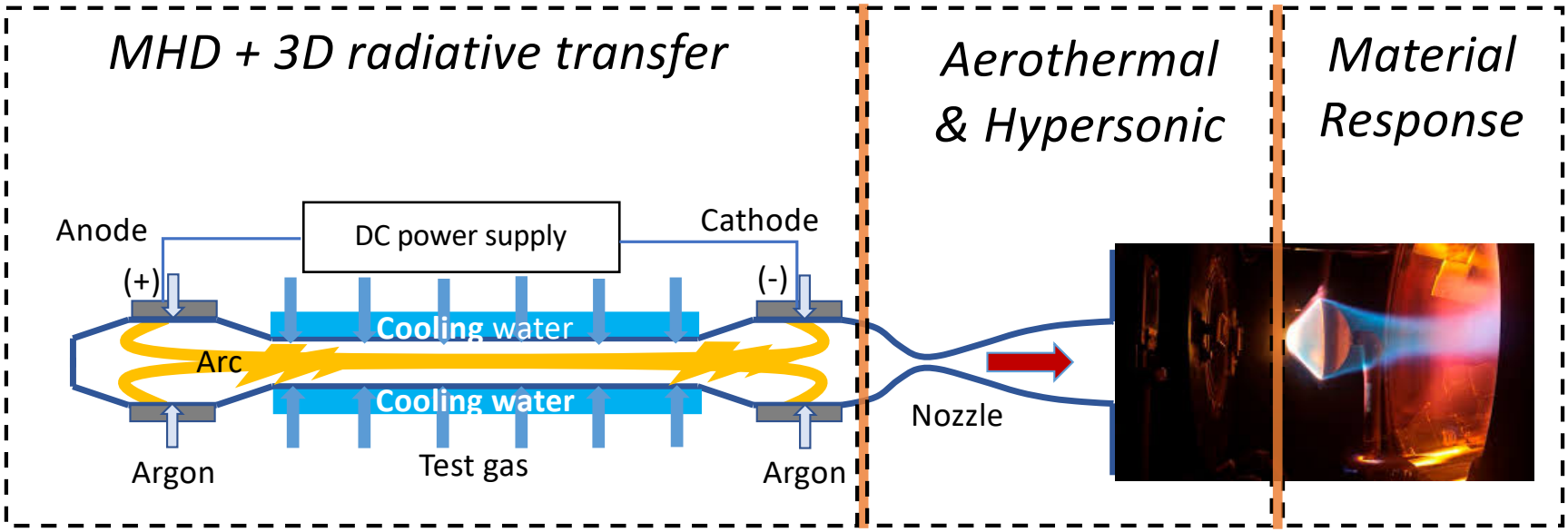

ARCHeS
ARC Heater Simulator

DPLR
Data-Parallel Line Relaxation

PATO
Porous-material Analysis Toolbox based on OpenFOAM

Part 1

High-fidelity modeling of arc heaters

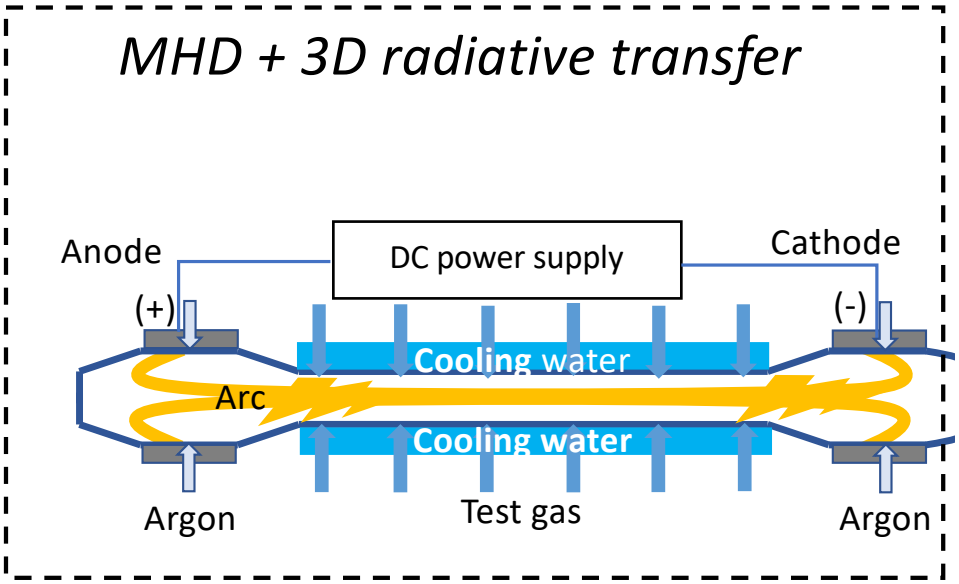

ARCHeS

ARC Heater Simulator

High-fidelity modeling of the **arc heaters**

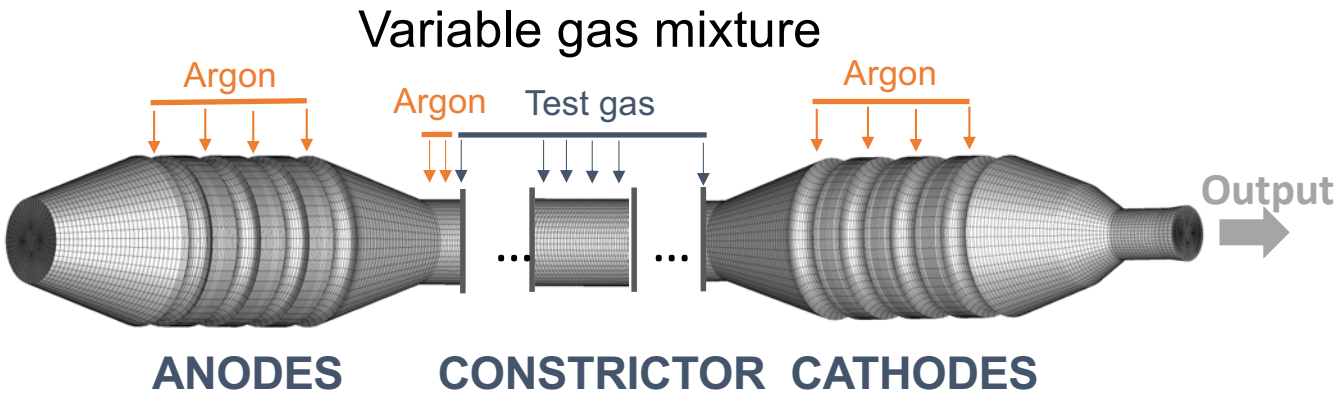

Swirl

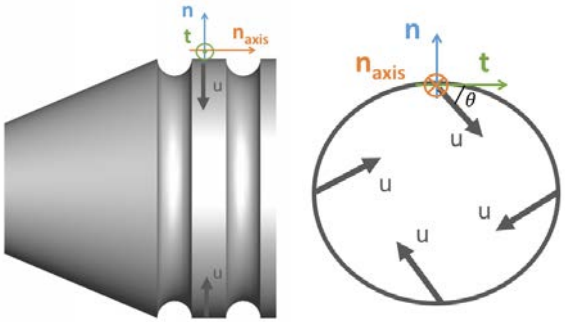

Internal magnetic drive

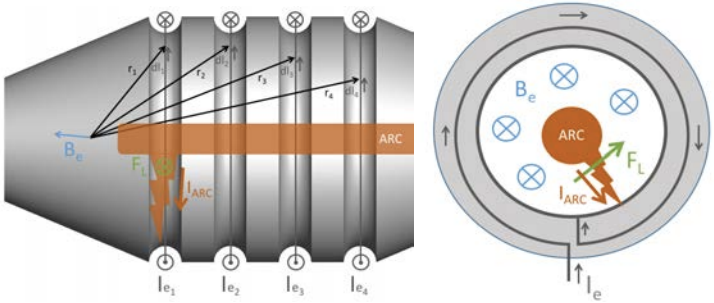

Electrical ballast

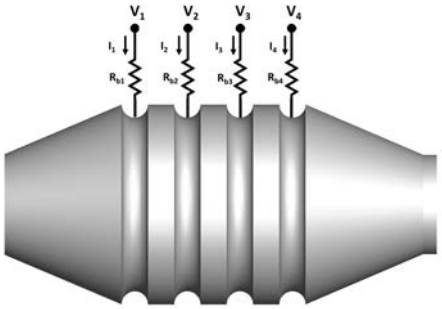

ARCHeS: ARC Heater Simulator [1]

Geometry concept

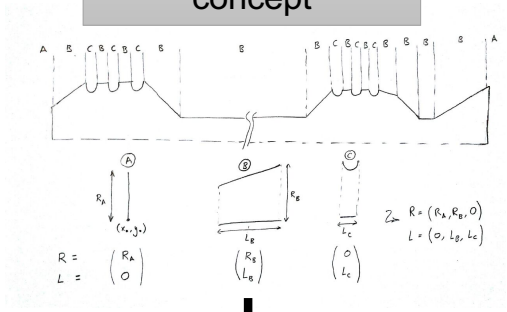

Automatic mesh inputs

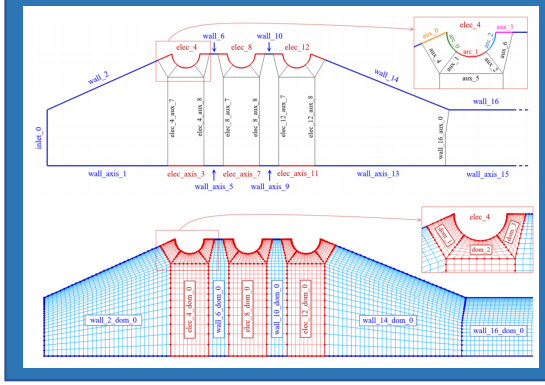

OpenFOAM

- Finite Volume
- I/O management
- Massive MPI
- Moving geometry
- Basic mesh gen.
- Mixture tables
- Chemistry
- Thermo/Transp.
- Turbulence
- Compressible flow
- Radiation

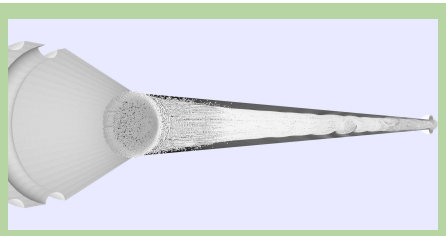

ARCHeS

MHD + ballast BC

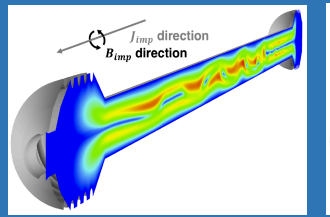

3D radiative transfer

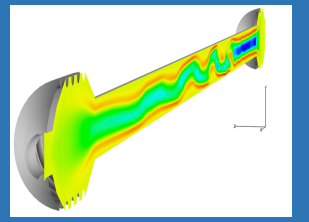

Complex mesh generation

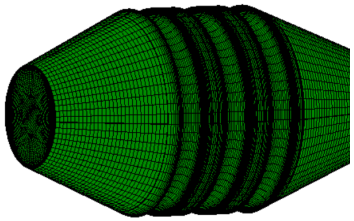

Thermo/Transport/ Chemistry

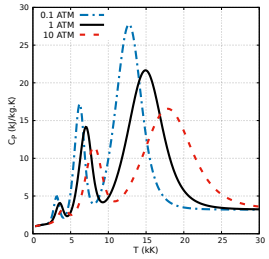

Post-processing 1D/2D/3D

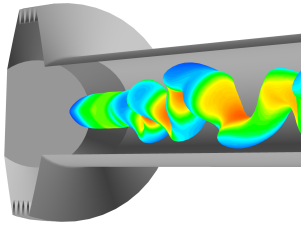

Modeling the **plasma**

FLOW CONDITION	$U_{avg} \approx 400$ m/s	$P_{avg} \approx 13$ atm	$T_{avg} \approx 8000$ K
ELECTROMAG.	$I_{avg} \approx 1200$ A	$B_{avg} \approx 0.2$ T	$\sigma_{avg} \approx 0.1$ S/m

$$S = \frac{L\, v_A}{\eta} = \frac{L\, \frac{B}{\sqrt{\rho \mu_0}}}{\eta} = 10^{-5}$$

High Lundquist numbers indicate **highly conducting** plasmas.
Low Lundquist numbers indicate **more resistive** plasmas.

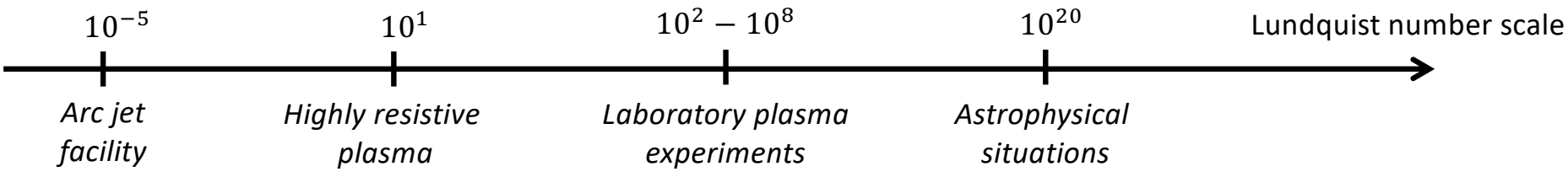

Electromagnetic model

$S = \frac{L\, v_A}{\eta} = 10^{-5}$ ⟶ The magnetic convection is negligible

$\mathbf{J} = \sigma \mathbf{E}$ ⟶ The Ohm's law is simplified

$\boldsymbol{\partial}_\mathbf{x} \times \mathbf{B} = \mu_0 \mathbf{J}$ ⟶ The displacement current is ignored ($V_0 << c$)

$\mathbf{B} = \boldsymbol{\partial}_\mathbf{x} \times \mathbf{A}$ ⟶ The vector potential formulation ensures zero divergence of the **B** field

$\boldsymbol{\partial}_\mathbf{x} \cdot \mathbf{J} = 0$ ⟶ Diverge of Ampere's law gives the continuity of current

$-\boldsymbol{\partial}_\mathbf{x}^2 \mathbf{A} = \mu_0 \mathbf{J}$ ⟶ Rotational of Ampere's law simplifies the equation

$$\begin{cases} \boldsymbol{\partial}_\mathbf{x} \cdot (-\sigma \boldsymbol{\partial}_\mathbf{x} \phi_i) = 0 \\ \boldsymbol{\partial}_\mathbf{x}^2 \mathbf{Ai} - \mu_0 \sigma \boldsymbol{\partial}_\mathbf{x} \phi_i = 0 \end{cases}$$ ⟶ System of electromagnetic equations solved in ARCHeS

Multiphysics model

MASS	$\partial_t \rho + \boldsymbol{\partial_x}.(\rho \mathbf{u}) = 0$
MOMENTUM	$\partial_t(\rho \mathbf{u}) + \boldsymbol{\partial_x} . (\rho \mathbf{u}\mathbf{u}) = - \boldsymbol{\partial_x} p + \boldsymbol{\partial_x} . \bar{\bar{\boldsymbol{\tau}}} + \mathbf{J} \times \mathbf{B}$
ENERGY	$\partial_t(\rho E_0) + \boldsymbol{\partial_x} . (\rho H_0 \mathbf{u}) = \boldsymbol{\partial_x} . (\bar{\bar{\boldsymbol{\tau}}} . \mathbf{u} + \mathbf{q}^{cond}) + \sigma \lvert \mathbf{E} \rvert^2 + \mathbf{u} . (\mathbf{J} \times \mathbf{B}) - \boldsymbol{\partial_x} . \mathbf{q}^{rad}$
IMPOSED CURRENT	$\boldsymbol{\partial_x} . (-\sigma \boldsymbol{\partial_x} \phi_i) = 0 \qquad \mathbf{E_i} = - \boldsymbol{\partial_x} \phi_i \qquad \mathbf{J_i} = \sigma \mathbf{E_i}$
IMPOSED MAGNETIC	$\boldsymbol{\partial_x^2} \mathbf{A_i} - \mu_0 \sigma \boldsymbol{\partial_x} \phi_i = 0 \qquad \mathbf{B_i} = \boldsymbol{\partial_x} \times \mathbf{Ai}$
EXTERNAL MAGNETIC	$\mathbf{A_e} = \frac{\mu_0 I_e}{4\pi} \oint \frac{\boldsymbol{dl}}{\lvert \boldsymbol{r} - \boldsymbol{r'} \rvert} \qquad \mathbf{B_e} = \boldsymbol{\partial_x} \times \mathbf{A_e}$
TOTAL FIELD	$\mathbf{B} = \mathbf{B_i} + \mathbf{B_e} \qquad \mathbf{E} = \mathbf{E_i} \qquad \mathbf{J} = \mathbf{J_i}$
RADIATION	$\boldsymbol{n} . \boldsymbol{\partial_x} I_\lambda(\boldsymbol{x}, \boldsymbol{n}) = \kappa_\lambda(\boldsymbol{x})[B_\lambda(T) - I_\lambda(\boldsymbol{x}, \boldsymbol{n})]$

Efficient Variable Mixture Multi-Band **Radiation** Model [2]

P.O.C.: Sergio Fraile Izquierdo

Two major approximations assumed:

- Medium in Local Thermodynamic Equilibrium (LTE)
- Scattering was neglected

NEQAIR was used to calculate the absorption coefficients for variable LTE air-argon mixtures

- F(T, p, χ)
- M++ (equilibrium)
- 13 species (Air13)
- λ = 0.04 - 20 μm
- 550,000 $\Delta\lambda$

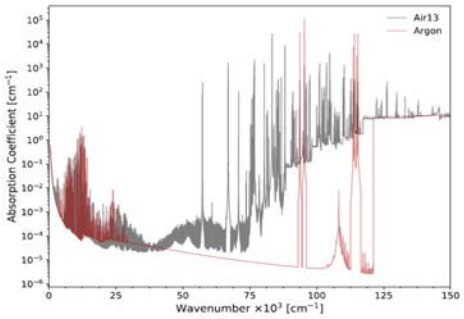

Fig. 1 Spectral absorption coefficients for LTE air and argon at 10,000 K and 1 atm

Radiative Transfer Equation (RTE):

$$\hat{n} \cdot \nabla I_\lambda(\vec{x}, \hat{n}) = \kappa_\lambda(\vec{x}) \left[B_\lambda(T) - I_\lambda(\vec{x}, \hat{n}) \right]$$

Radiative Heat Flux:

$$q(\vec{x}) = \int_0^\infty \int_\Omega I_\lambda(\vec{x}, \hat{n})\, \hat{n}\, d\Omega\, d\lambda$$

The multi-band method: reduces the spectrum into groups of wavelengths defining a mean absorption coefficient for each group or band:

$$\tilde{\kappa}_b = \kappa_{P_b} = \frac{\int_{\lambda_1}^{\lambda_2} \kappa_\lambda B_\lambda \, d\lambda}{\int_{\lambda_1}^{\lambda_2} B_\lambda \, d\lambda}$$ ➢ **Planck MAC**

$$\tilde{\kappa}_b = \kappa_{R_b} = \frac{\int_{\lambda_1}^{\lambda_2} \frac{\partial B_\lambda}{\partial T} d\lambda}{\int_{\lambda_1}^{\lambda_2} \frac{1}{\kappa_\lambda} \frac{\partial B_\lambda}{\partial T} d\lambda}$$ ➢ **Rosseland MAC**

$$\tilde{\kappa}_b = \kappa_{BPR_b} = \sqrt{\kappa_{P_b} \kappa_{R_b}}$$ ➢ **Blended-PR MAC**

Efficient Variable Mixture Multi-Band **Radiation** Model [2]

P.O.C.: Sergio Fraile Izquierdo

Radiative Heat Transfer model:

- **LBL**: very accurate & expensive.
- **Planck and Rosseland**: high error at low number of bands and cost-effective.
- **Blended-PR**: low error at low number of bands and cost-effective.

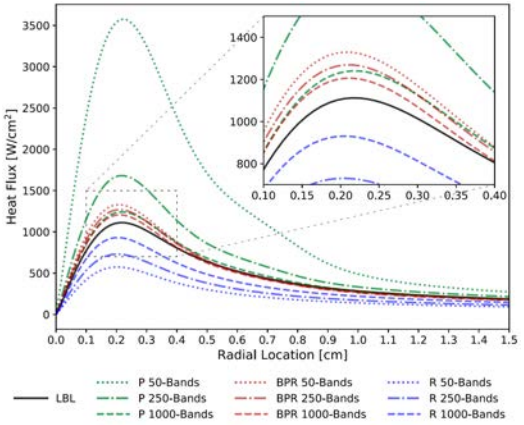

Fig. 1 Heat flux profiles for LBL and different banding models at 10 atm

Variable Air-Argon mixture model:

- Capability to compute variable Air-Argon mixtures on the fly
- Spectral properties of air-argon mixtures can be estimated from air and argon's data.

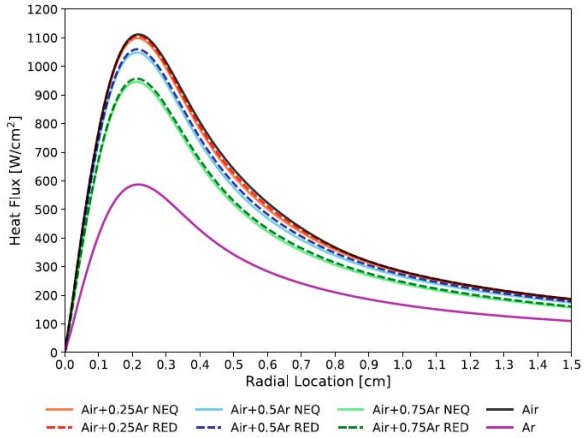

Fig. 2 Heat flux profiles for air-argon mixtures computed LBL and using the reduced model at 10 atm

Efficient 3D radiative transport
advance order method

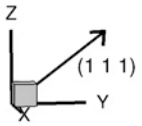

$$I_{\upsilon,c}^{d} = \frac{\sum_{k_i}^{N_{k_i}} I_{\upsilon,k_i}^{d}\ \Omega_d \,.\, \Delta S_c .+ \kappa_{\upsilon,c}\ B_{\upsilon,c}\ V_c}{\sum_{k_o}^{N_{k_o}} I_{\upsilon,k_o}^{d}\ \Omega_d \,.\, \Delta S_c .+ \kappa_{\upsilon,c}\ V_c}$$

$$\partial_x \,.\, q^{rad} = \sum_{\upsilon}^{N_b} \sum_{d}^{N_d} \frac{a_d\, I_{\upsilon,c}^{d}\, \Omega_d \,.\, \Delta S_c}{V_c}$$

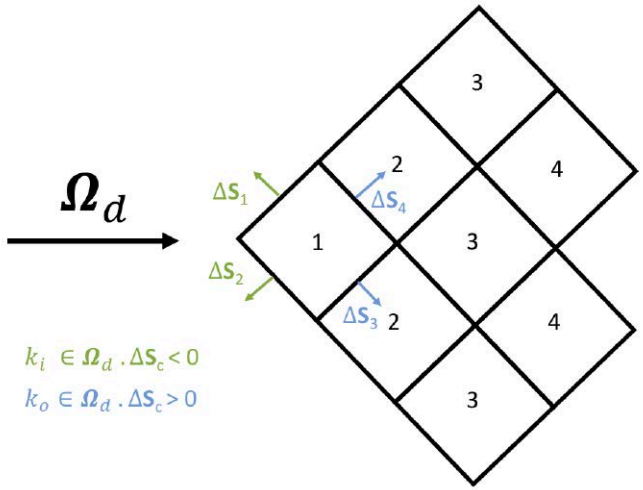

Capturing the electric **arc instabilities**

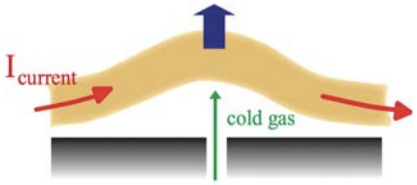

Thermal instability

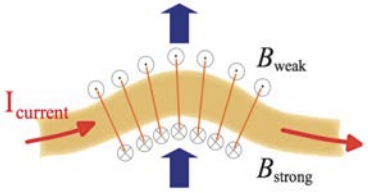

Kink instability

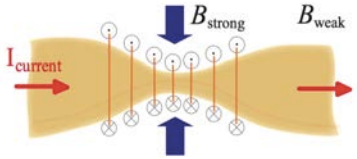

Sausage instability

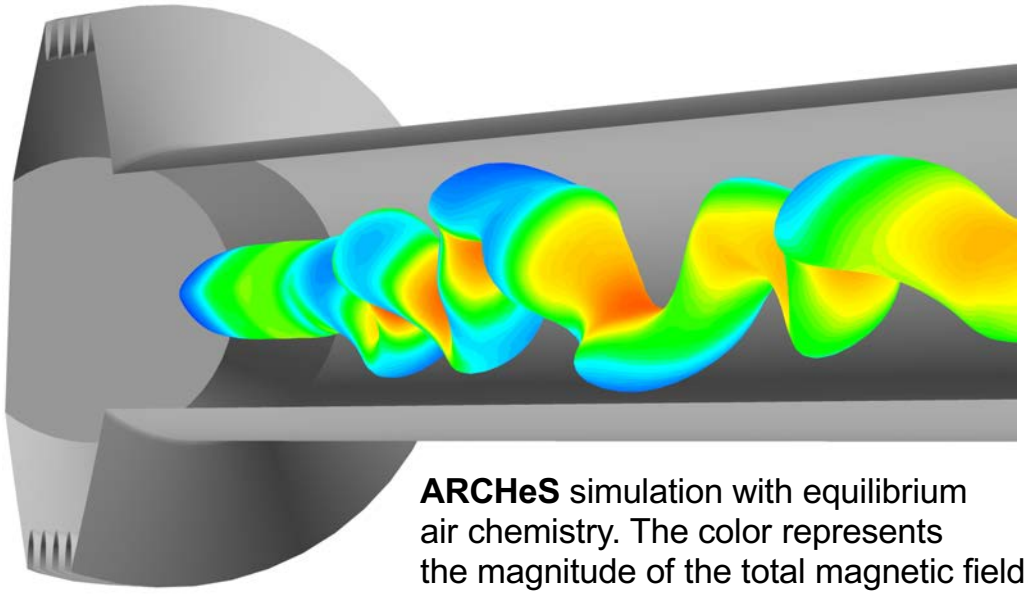

ARCHeS simulation with equilibrium air chemistry. The color represents the magnitude of the total magnetic field. Iso-surface of the current density of 1 MA/m^2.

Stable arc next to the electrode chambers. Instablilities arise in the constrictor.

Temperature and **radiation** results

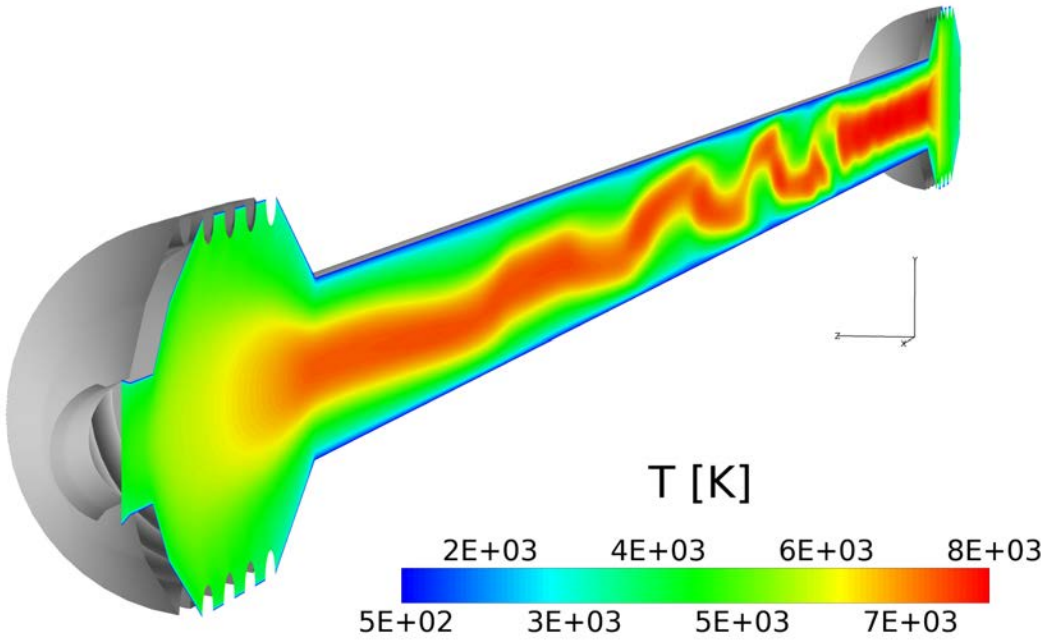

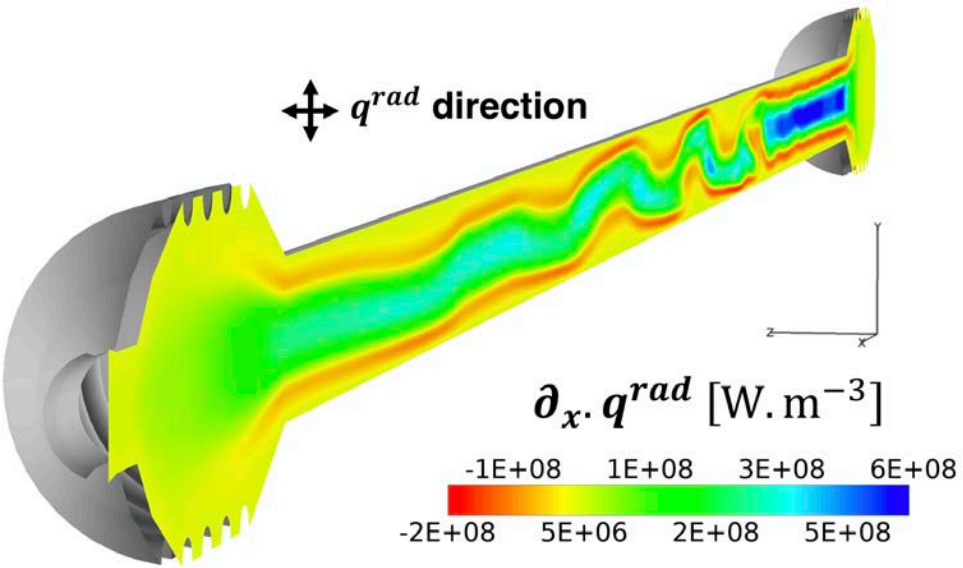

Hot electric arc core cools down and the surroundings warm up.
Importance of the 3D radiative transfer.

Current density and **magnetic field** intensity

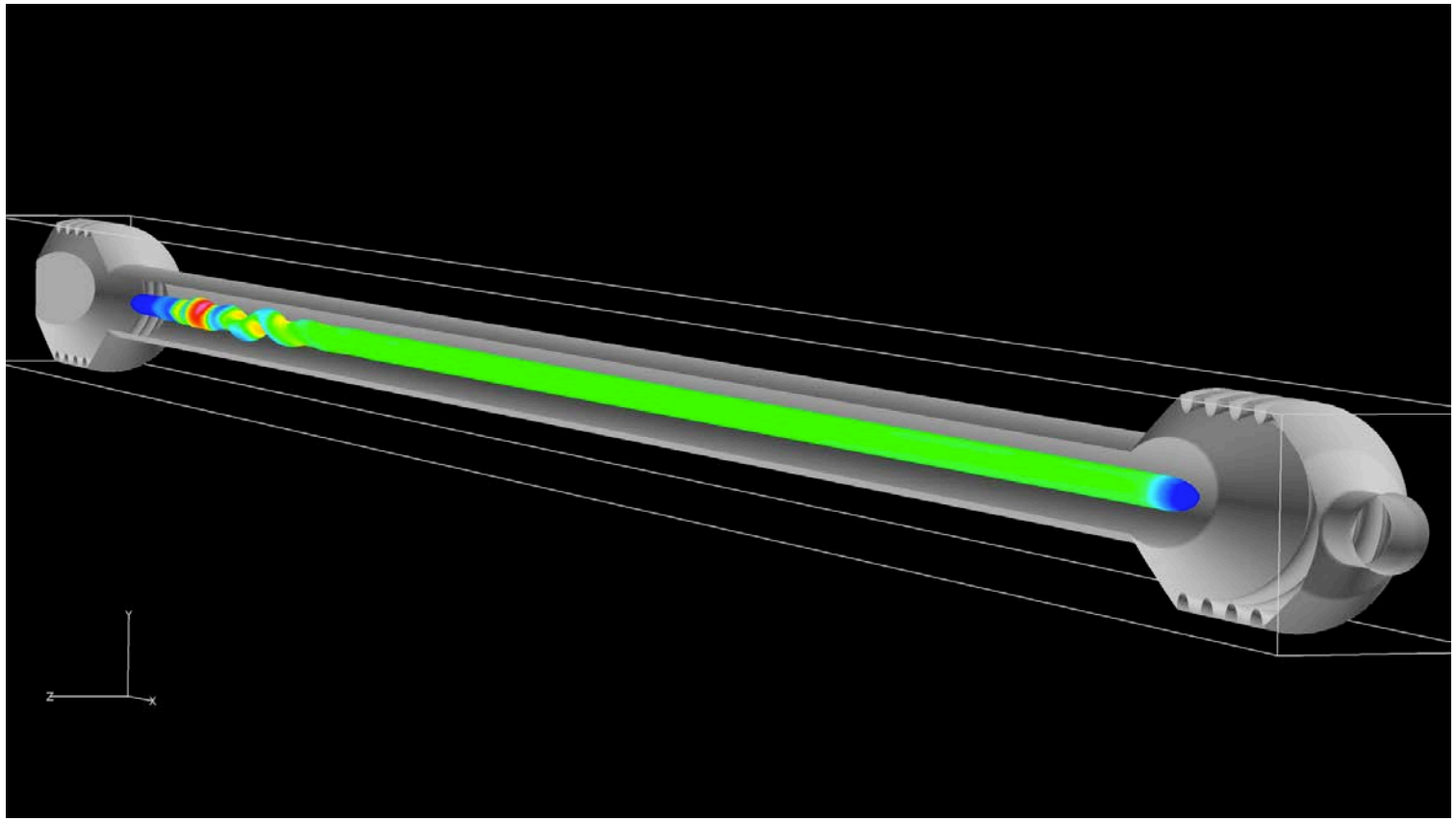

Arc attachment at the electrode

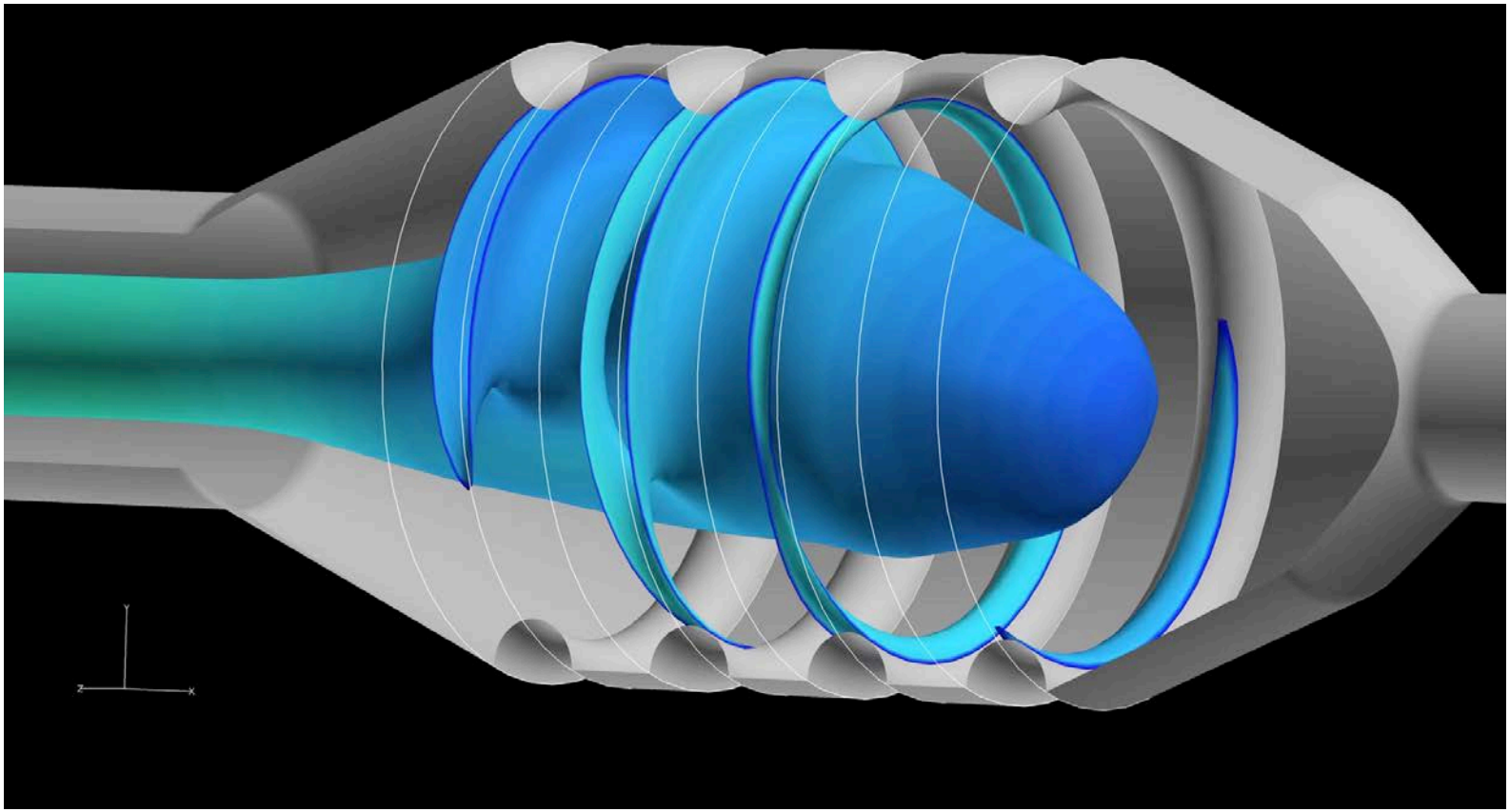

Argon mass fraction

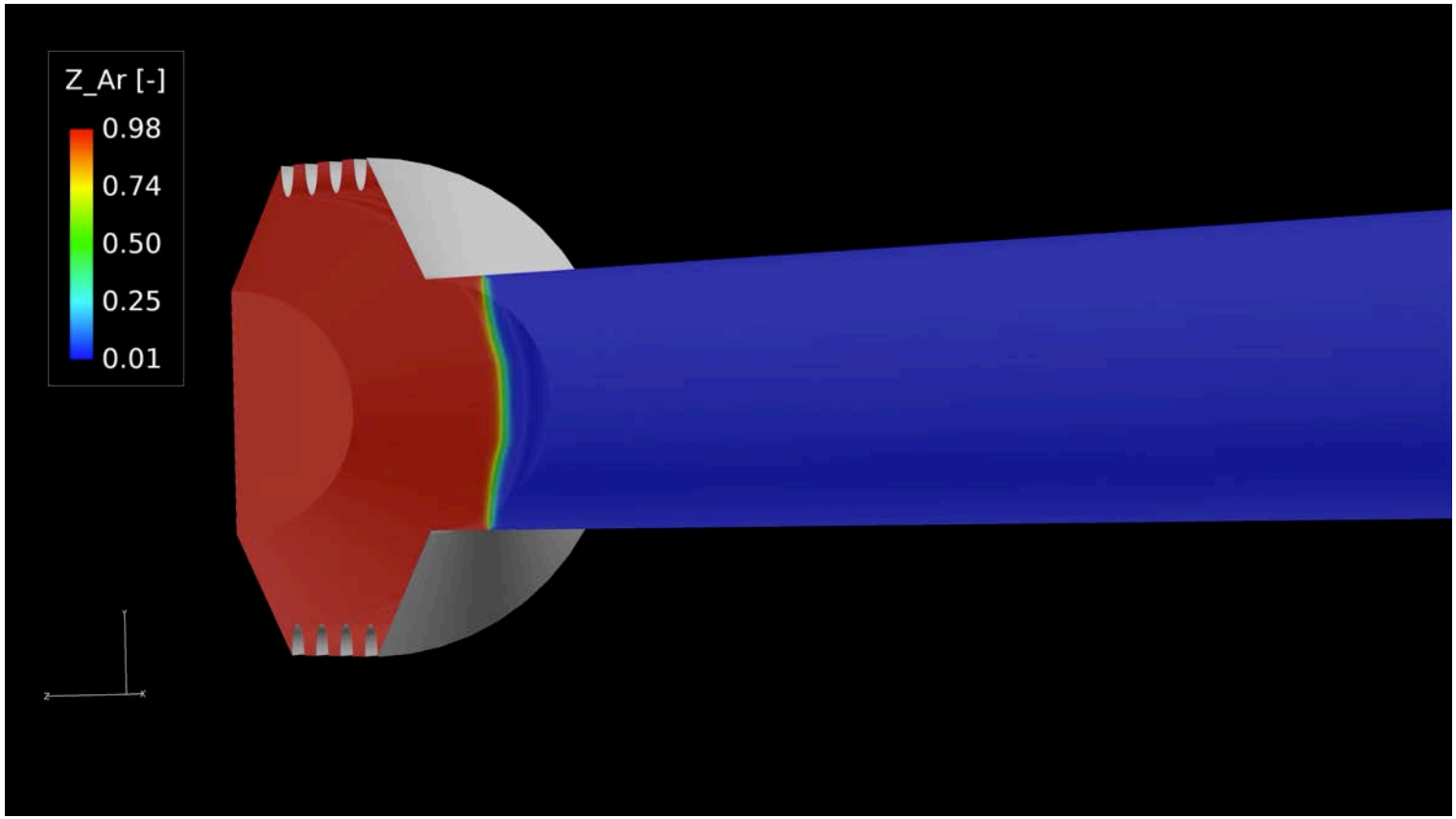

Impact of argon injection on **arc stability**

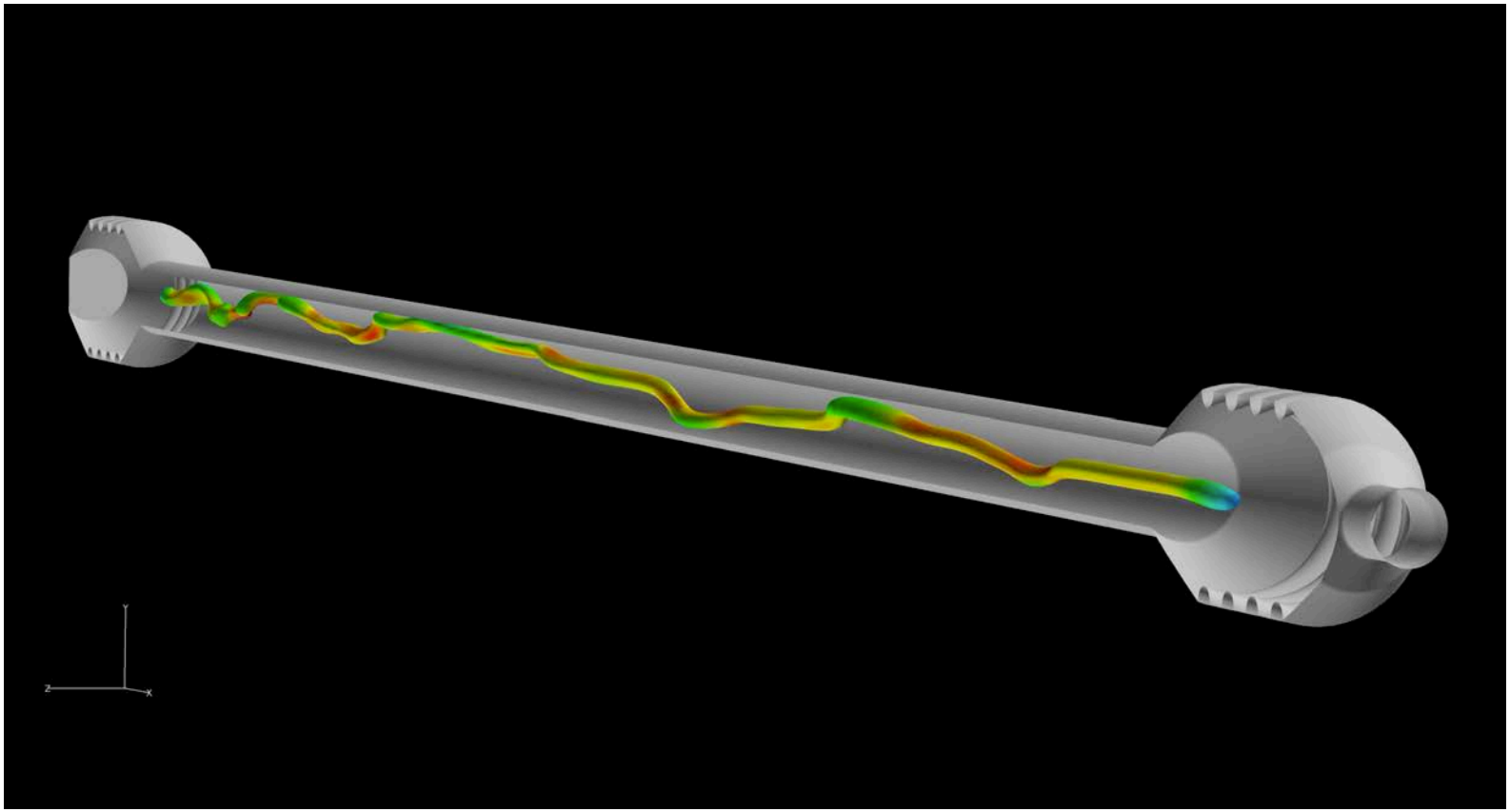

Experimental validation [3]

P.O.C.: Magnus Haw

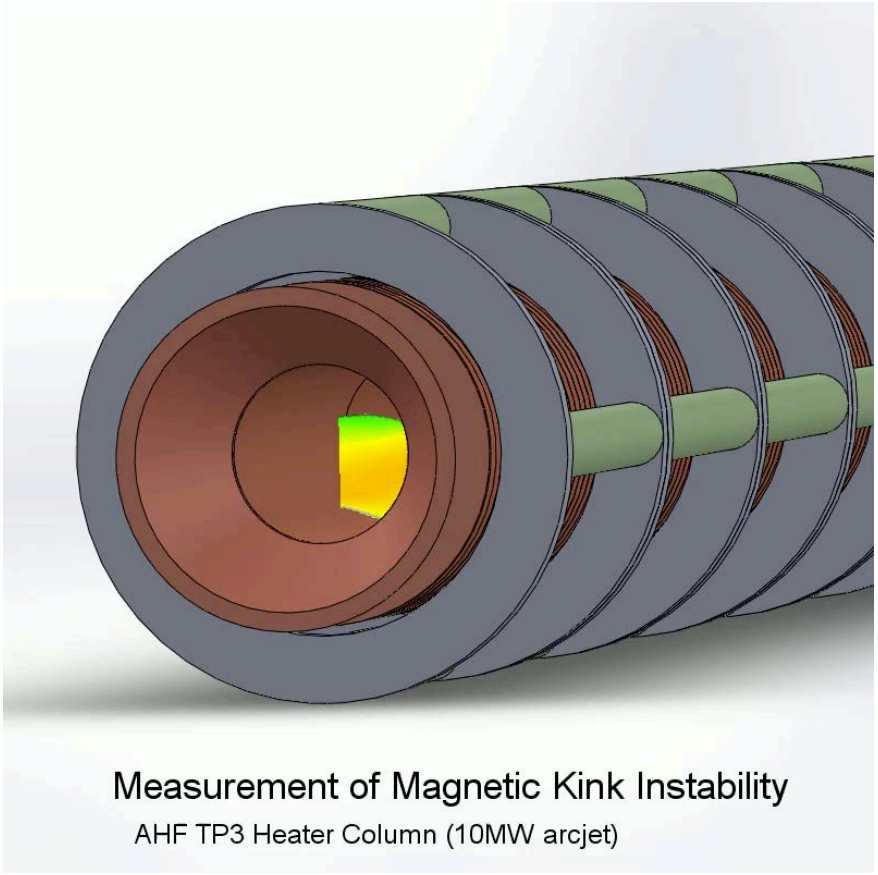

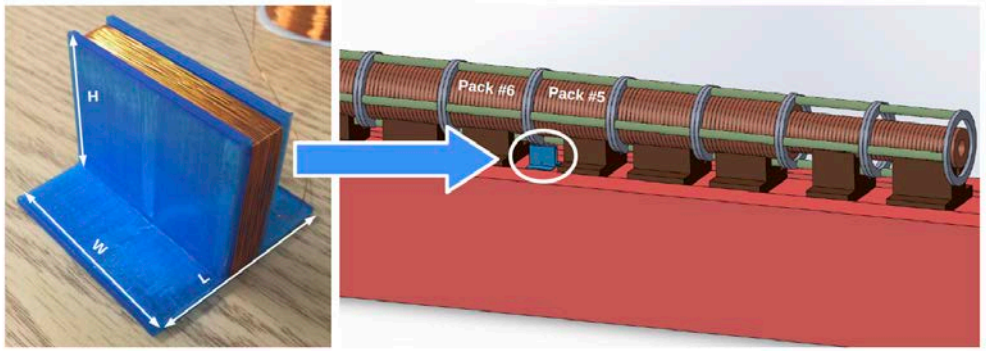

Fig. 1 Image of inductive coil sensor and coil placement below AHF heating column.

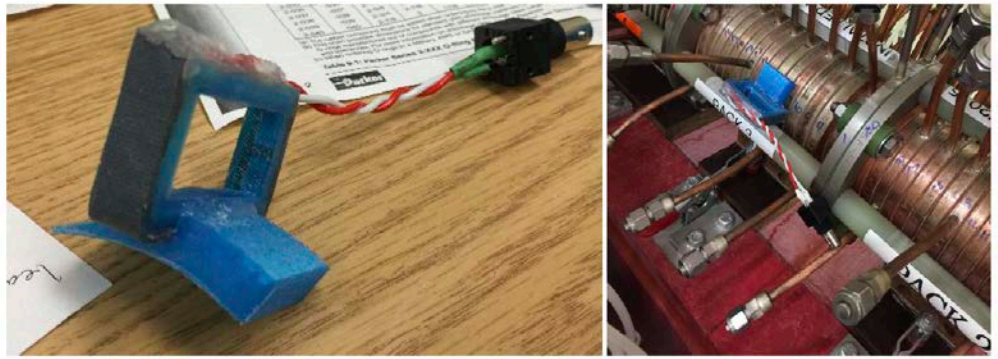

Fig. 2 (Left) Column mounted coil: rectangular coil with 100 turns of AWG 33 wire. 3D printed mount matches curvature of column and thin lower lip fits into the gap between the column and green tension bar. (Right) Coil mounted on Pack 3 of AHF 10 MW heater.

Part 2

High-fidelity modeling of arc-jet aerothermal environments

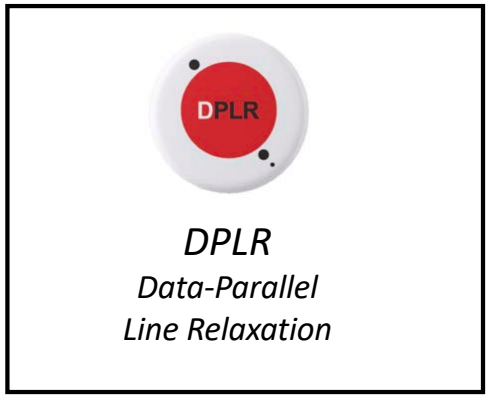

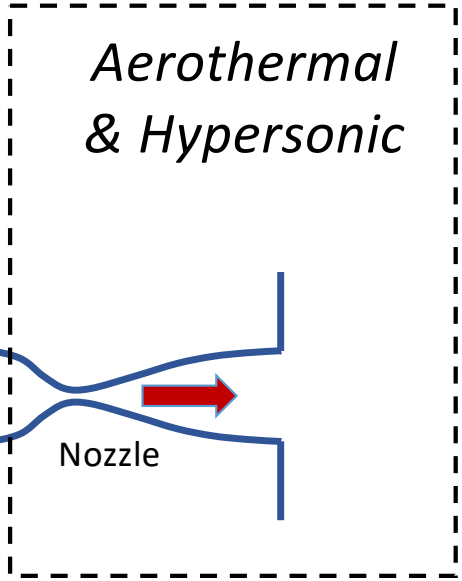

CFD/Machine Learning simulations [4]

P.O.C.: Patricia Ventura Diaz

Generating database for ML

1. Given $\dot{m}$ for each p_i & h_i

2. **Mutation++:** Compute inflow variables

3. **DPLR**: Stag. point CFD solution each q_w & p_w

ML

4. **Scikit-learn**: Find $[p_i , h_i]$ for $q_{w,exp}$ & $p_{w,exp}$

High-fidelity CFD

5. **Mutation++**: Compute inflow variables

6. **DPLR**: Stag. point CFD solution each q_w & p_w

7. **BLAYER**: Compute the BLE envi. C_H, h_e & p_w

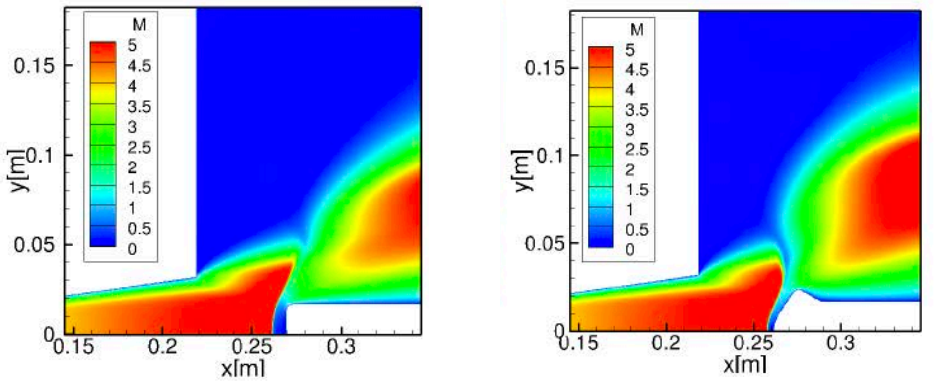

Fig. 1 Mach number contours using Earth atmosphere.

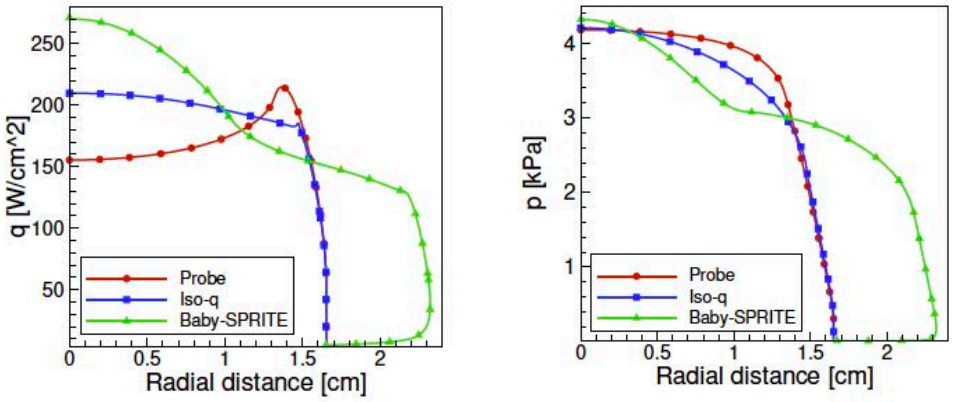

Fig. 2 Distribution of heat flux (left) and pressure (right).

Part 3

High-fidelity material response modeling

PATO

Porous-material Analysis Toolbox based on OpenFOAM

Material Response

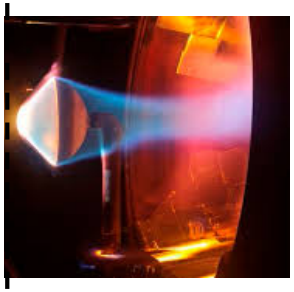

Porous material Analysis Toolbox based on OpenFOAM [5,6,7]

PATO overview

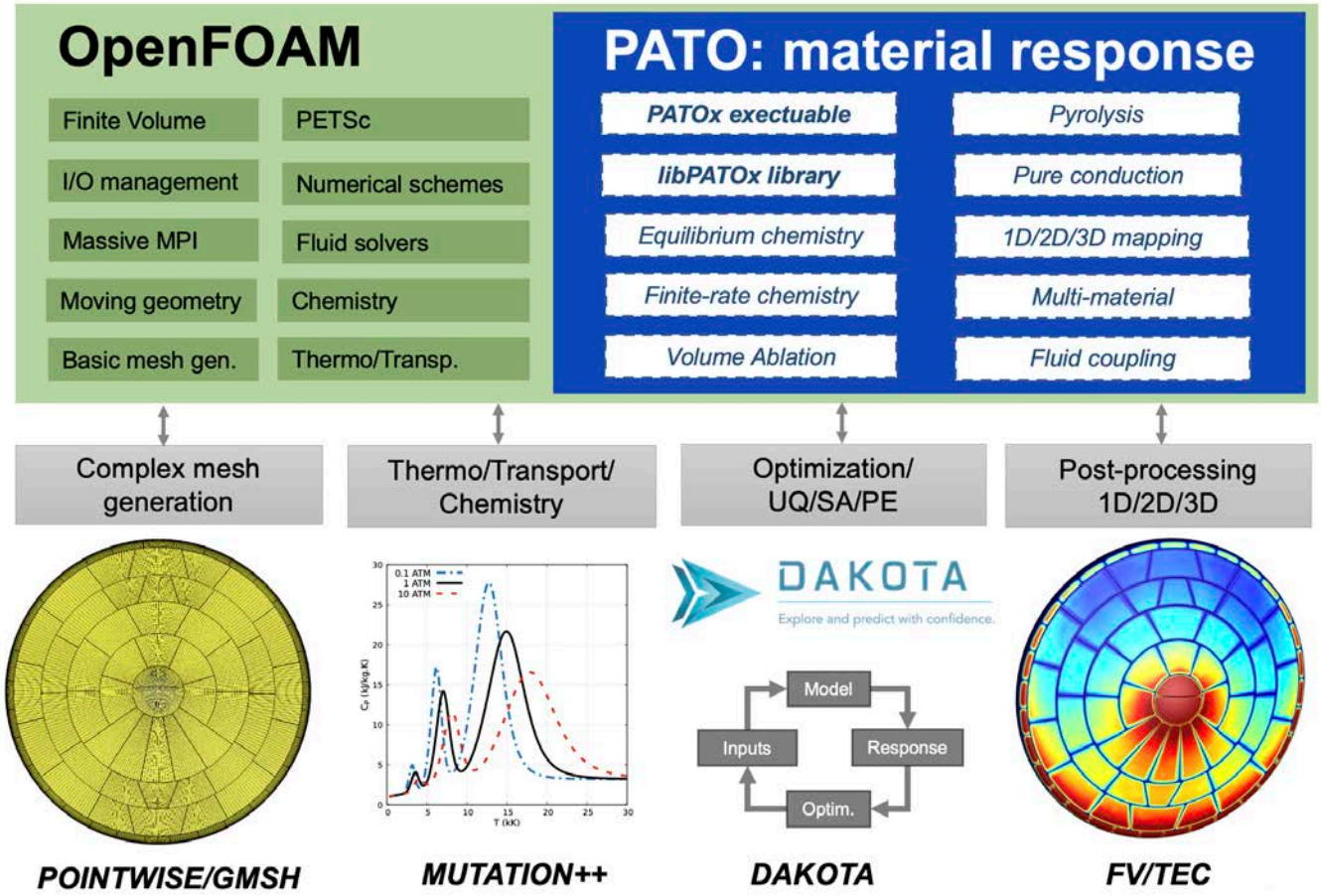

More info on PATO

- *PATO website:*
  - http://www.pato.ac/
- *Private gitlab:*
  - gitlab.com/PATO/PATO-dev
- *PATO module on PFE*
  - module use -a /u/jmeuriss/modulefiles
  - module load PATO/dev
  - module load dakota/6.7
  - module load cmake/3.9
- *1D, 2D, 3D tutorials on PFE*
  - /u/jmeuriss/sharing/PATO/PATO-dev/tutorials
- *P.O.C. Jeremie Meurisse*
  - jeremie.b.meurisse@nasa.gov

MSL simulations using DPLR and PATO [7]

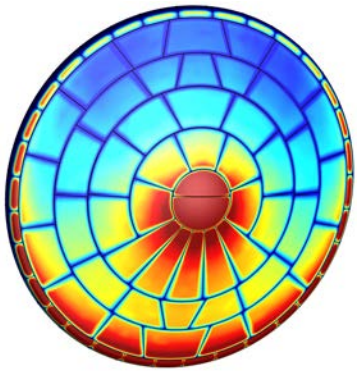

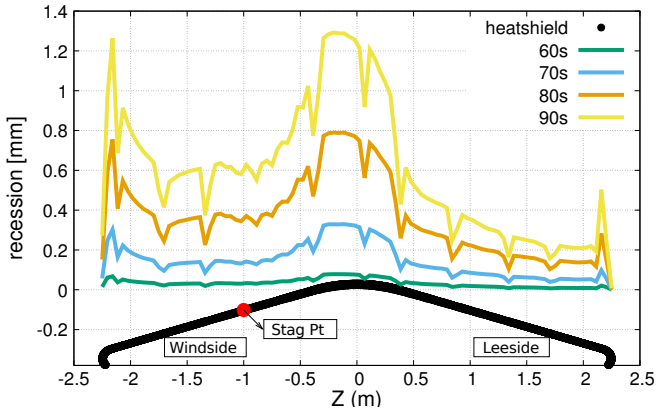

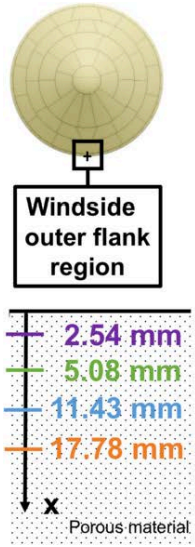

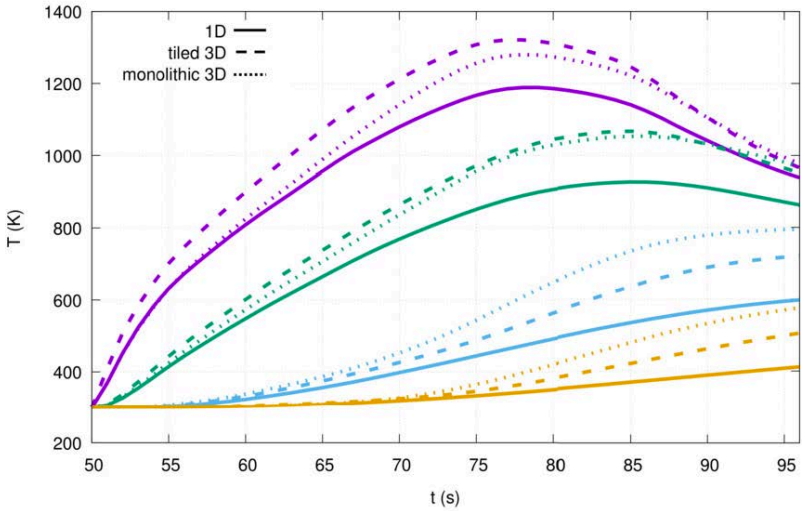

Fencing effect due to RTV between the tiles

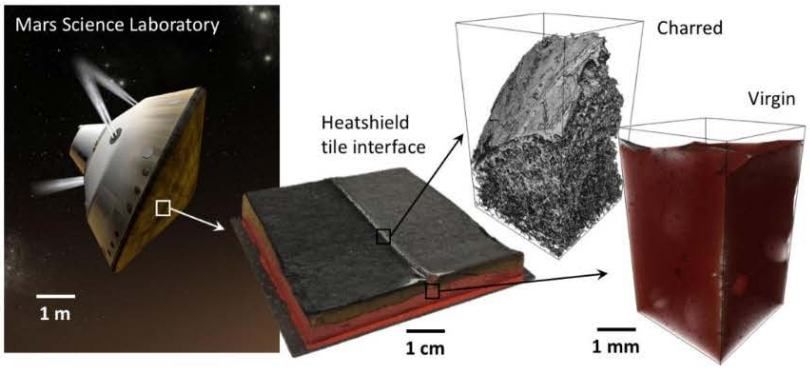

Coupling of the **pyrolysis** gas blowing [8]

P.O.C.: John Thornton

MISP4

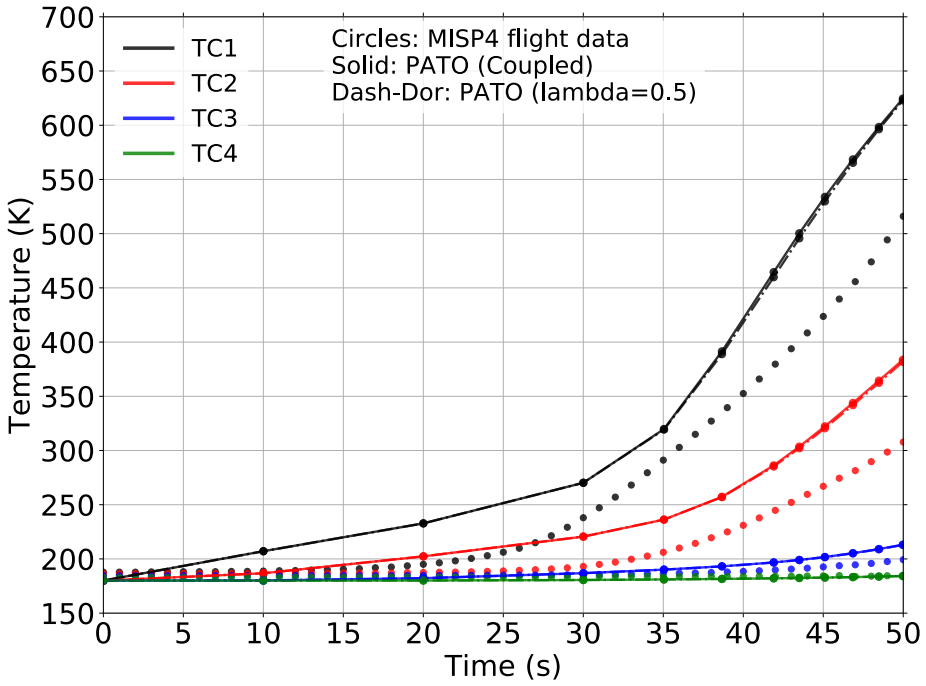

MISP6

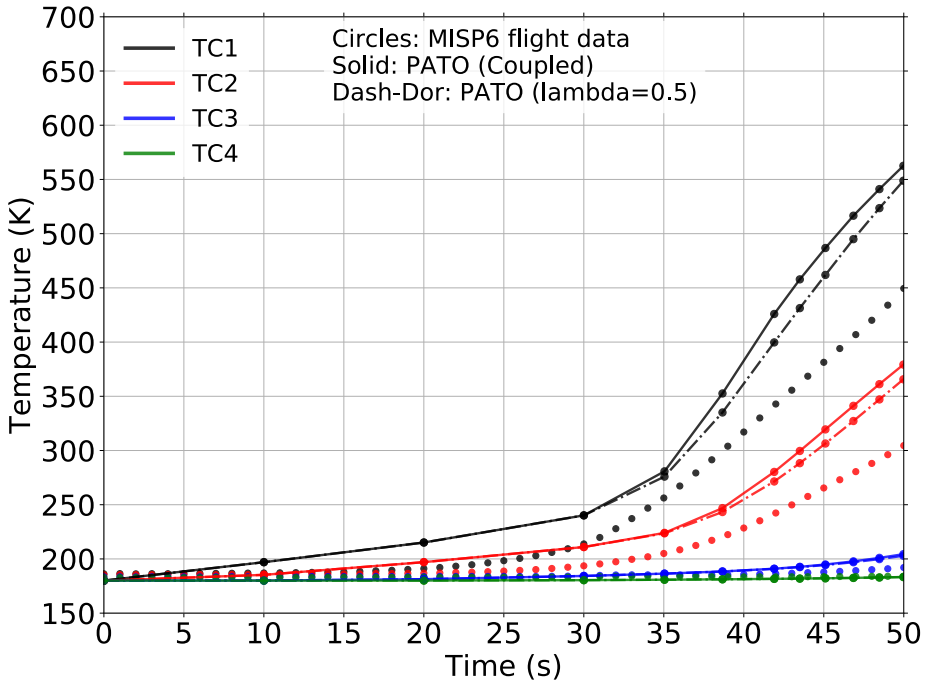

- PATO and DPLR coupling via the pyrolysis gas blowing.
- Environments up until 35 sec were provided from DSMC and were not coupled.
- Radiation computations from NEQAIR were added starting at 42 sec.

Coupling of the **pyrolysis** gas blowing [8]

P.O.C.: John Thornton

Temperature at 42 sec

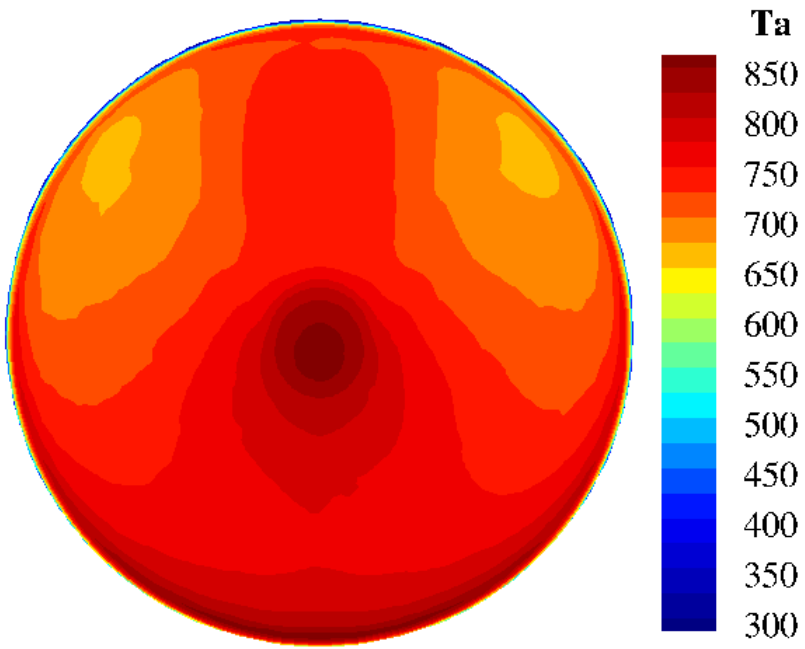

Pyrolysis gas blowing at 42 sec

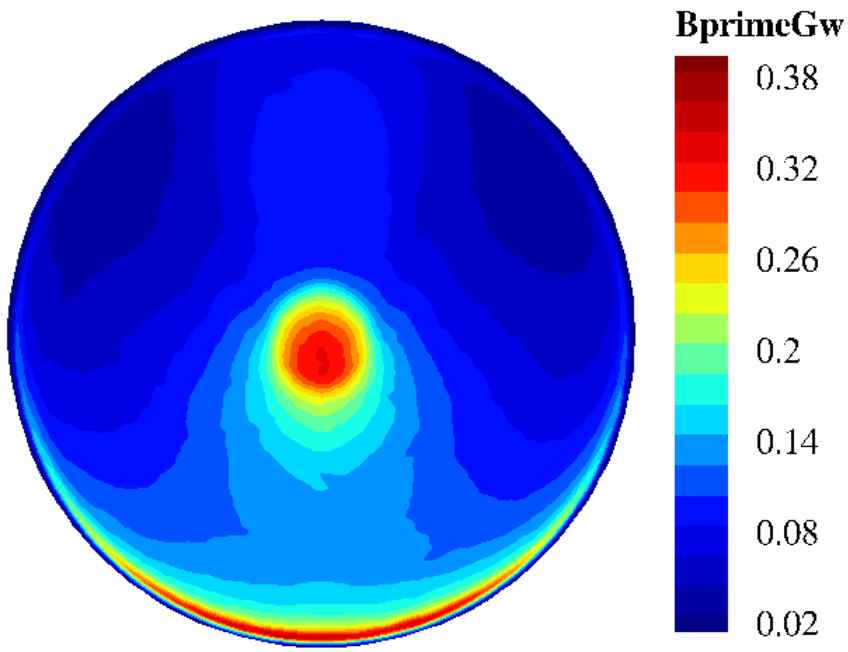

Calibration of the pyrolysis gases [9]

Oxygen

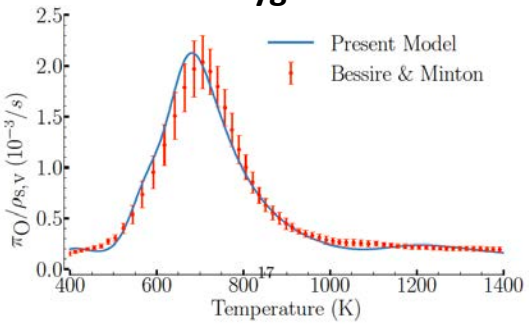

Hydrogen

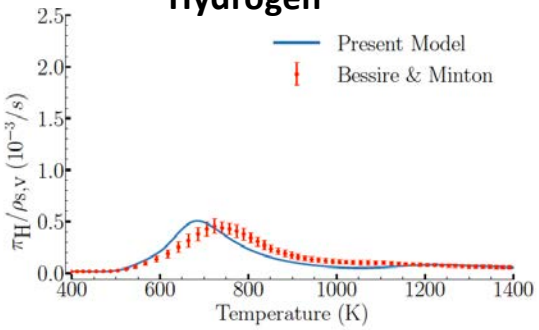

Carbon

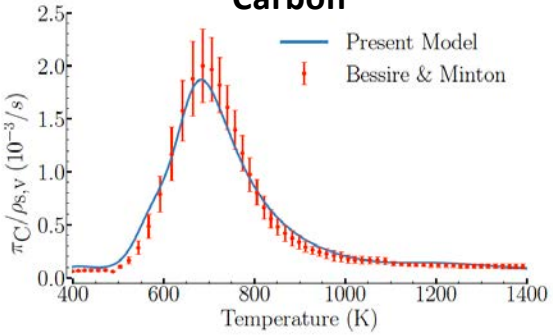

TGA curve

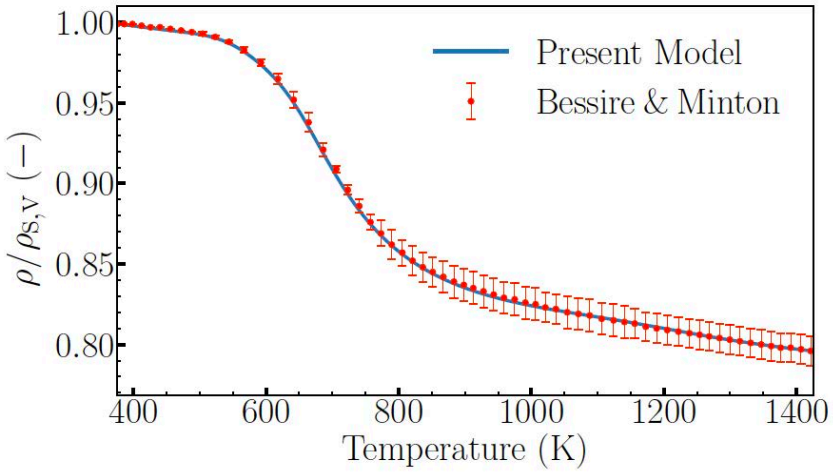

New pyrolysis model for PICA

R	F(-)	$\log(\mathcal{A})(s^{-1})$	$\mathcal{E}$(kJ/mol)	n (-)	ζ(-)	
1	0.032	5.67	51.4	7.74	C	0.32
					H	0.06
					O	0.62
2	0.089	7.02	87.4	4.02	C	0.40
					H	0.07
					O	0.53
3	0.336	7.03	103.7	4.33	C	0.42
					H	0.12
					O	0.46
4	0.086	6.9	194.4	9.25	C	0.25
					H	0.21
					O	0.54

Inverse analysis using Dakota and PATO [10,11]

P.O.C.: John Thornton

TC1 driver

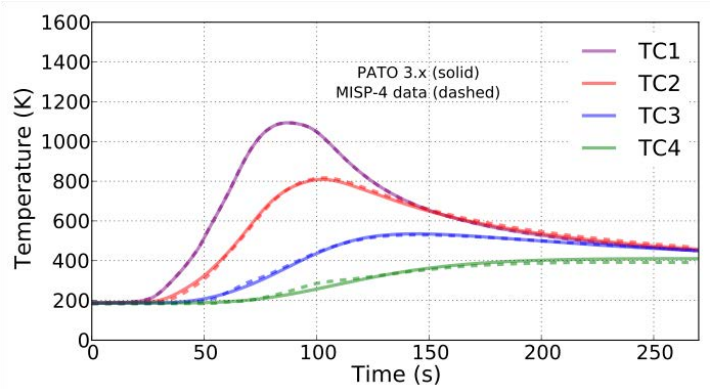

- **Estimation of material properties**
- Shallowest MISP4 thermocouple
- Imposed wall temperature
- Equilibrium chemistry
- Calibrated pyrolysis

Inverse environment

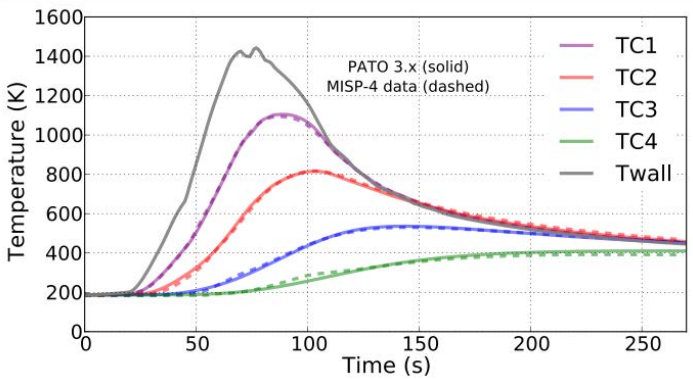

- **Estimation of surface convective heat flux and char ablation rate**
- Calculated temperature and recession using surface mass and energy balance
- Material properties from TC1 driver

Sensitivity analysis using Dakota and PATO

P.O.C.: John Thornton

Environment (MISP2 – TC2)

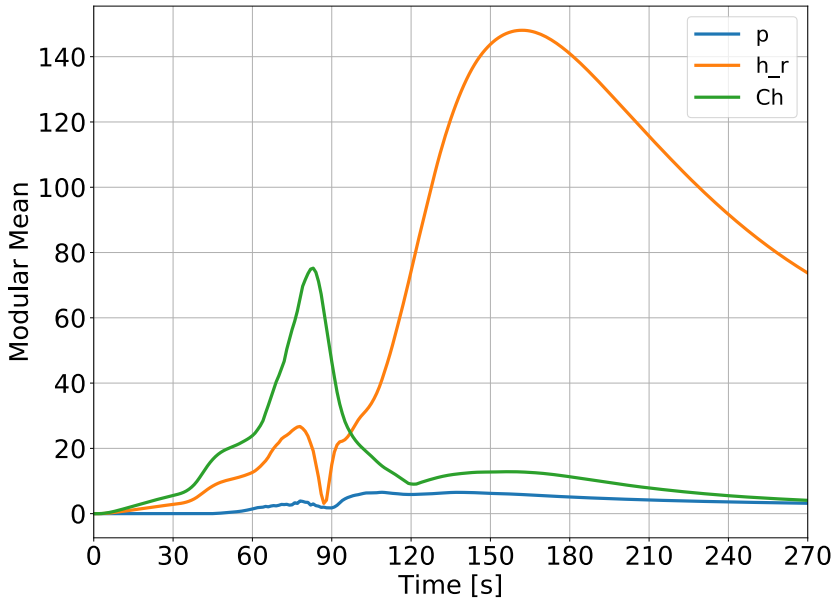

Material properties (MISP2 – TC2)

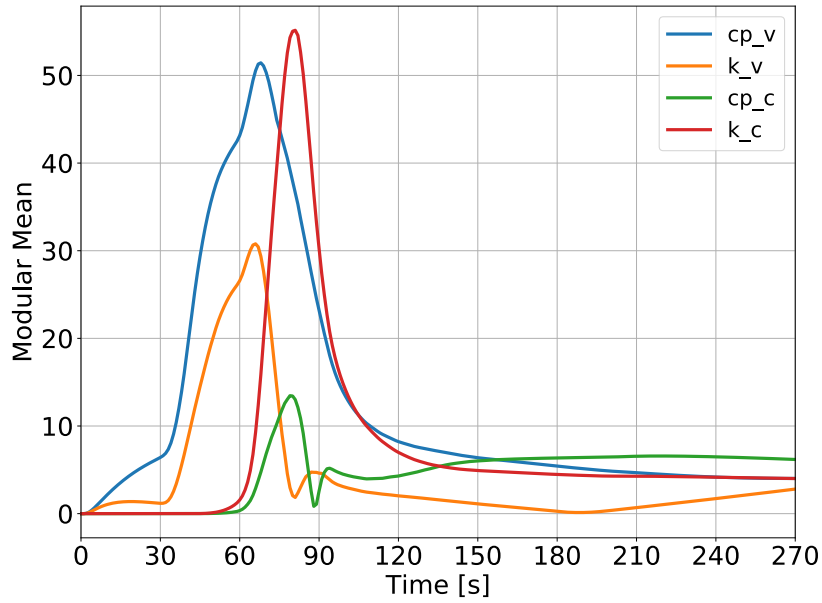

- Sensitivity of MSL response temperature to environment and material properties.
- Morris method in DAKOTA with PATO material response simulations for each MISP.
- Aerothermal environments obtained using DPLR (continuum) and SPARTA (rarefied).
- 1D material response simulations using PICA material properties.

Comparison between **FIAT** and **PATO** for **TACOT**

	pure **conduction** in the energy equation	**pyrolysis** gas in the mass and energy equations
tabulated temperature at the front surface	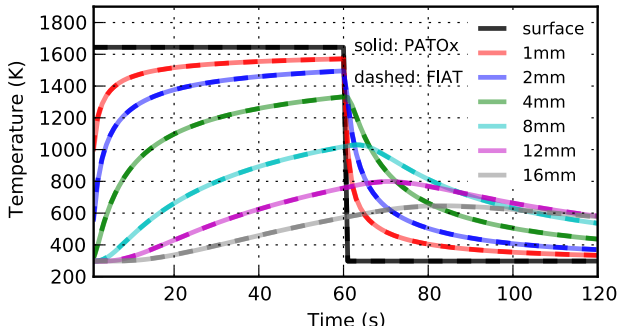	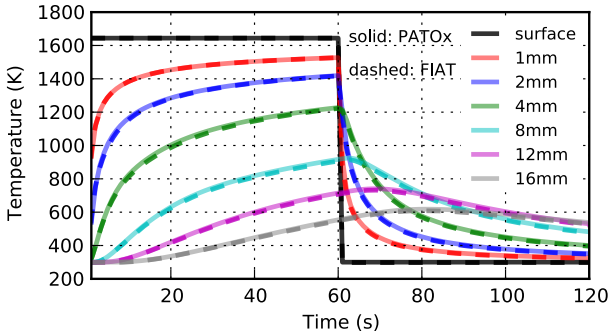
surface mass and energy **balance** at the front surface	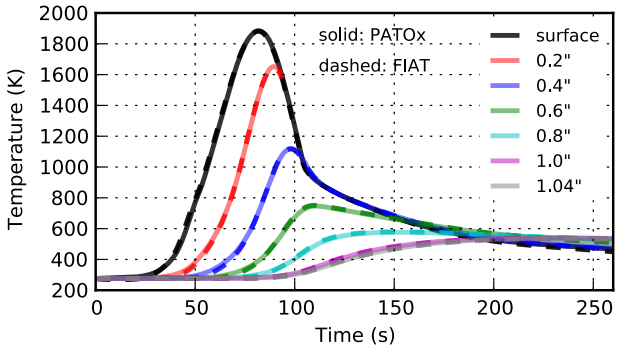	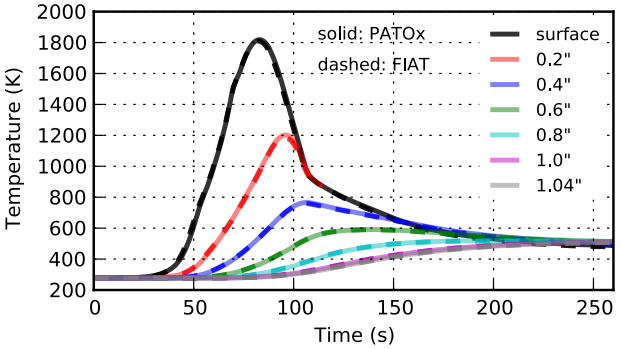

Full-fledged verification of PATO versus FIAT for TACOT

HyMETS test campaign – March 2019 [12,13]

P.O.C.: Brody Bessire

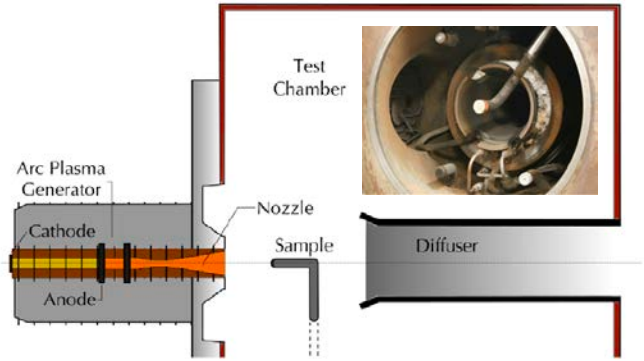

Fig. 1 Schematic view of HyMETS test section. [4]

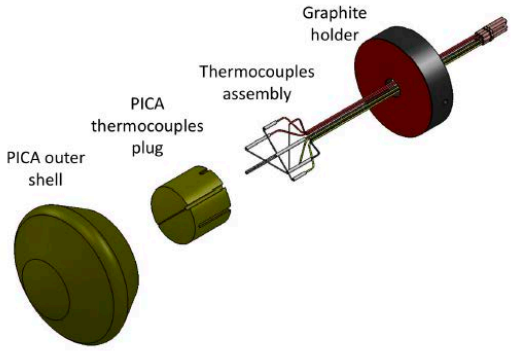

Fig. 2 Baby-SPRITE model assembly.

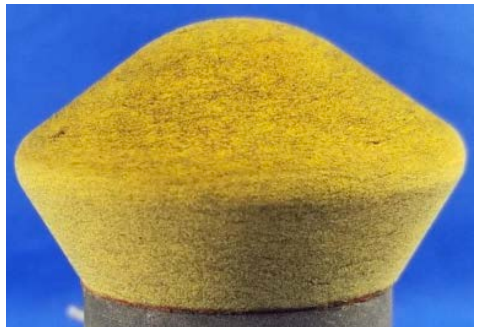

Fig. 3 Baby-SPRITE sample.

Material	Model	Atmosphere	Heat flux [W/cm²]	Pressure [kPa]
PICA-N	1	Earth	140	5.6
PICA-N	2	Earth	140	5.6
PICA-N	3	Earth	140	5.6
PICA-N	4	Earth	60	4.1
PICA-N	5	Earth	224	6.6
PICA-N	6	N_2	131	5.3

Material	Model	Atmosphere	Heat flux [W/cm²]	Pressure [kPa]
PICA-N	7	Mars	127	5.2
PICA-N	8	Earth	60	3.9
PICA	9	Earth	140	5.6
PICA	10	N_2	130	5.3
PICA	11	Earth	223	6.6
PICA	12	Mars	126	5.3

Material response simulations: CO_2 [12,15,16]

Material	Model	Atmosphere	Heat flux [W/cm²]	Pressure [kPa]
PICA	12	Mars	126	5.3

BLAYER: $p_w = 5.2\ kPa$ | $C_H = 0.19\ \frac{kg}{m^2 s}$ | $h_e = 6.7\ \frac{MJ}{kg}$

Recession: $r_{exp} = 5.69\ mm$ | $r_{pato} = 6.10\ mm$

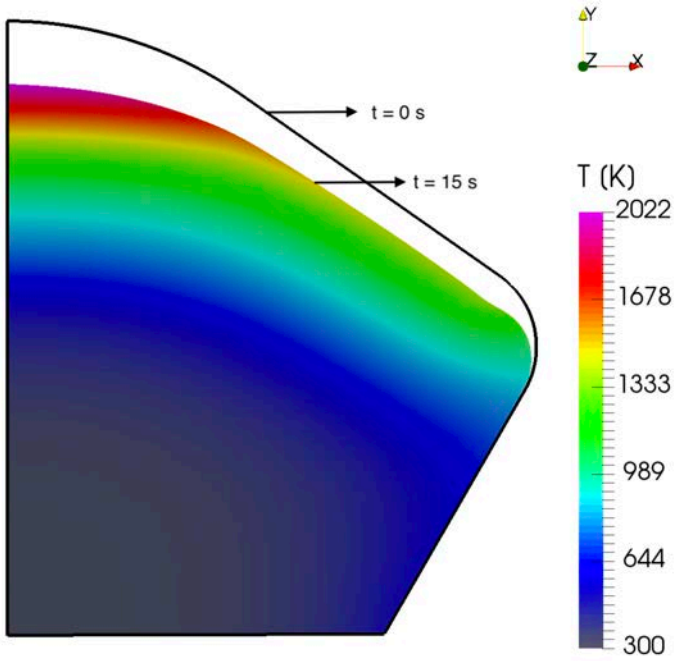

Fig. 1 Temperature and recession at 15 sec.

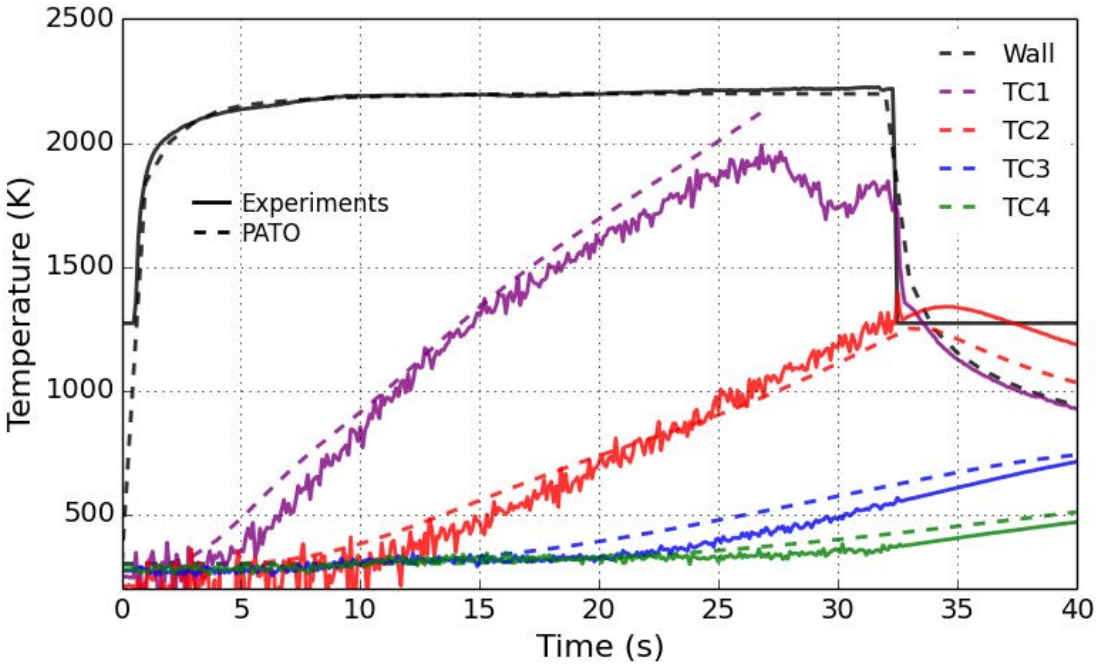

Fig. 2 Evolution in time of the temperature.

Summary

MHD + 3D radiative transfer

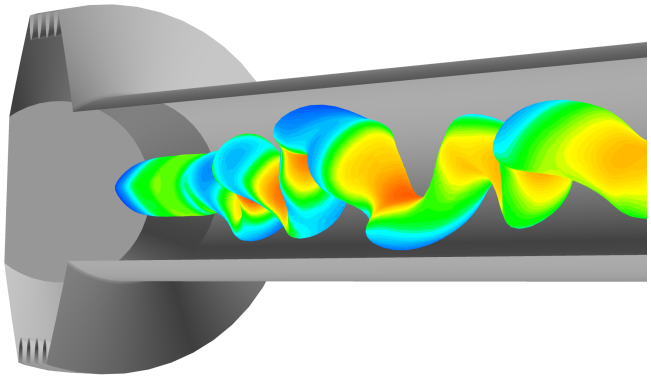

Aerothermal & Hypersonic

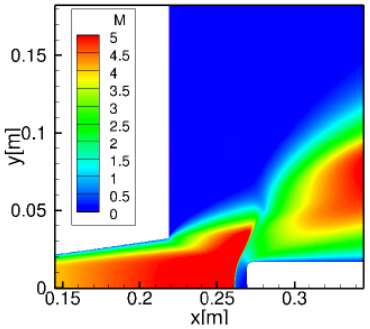

Material Response

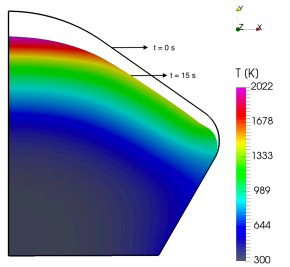

ARCHeS
ARC Heater Simulator

DPLR
Data-Parallel Line Relaxation

PATO
Porous-material Analysis Toolbox based on OpenFOAM

Acknowledgements

- *ARCHeS*: Joseph Schulz, Sander Visser and Alan Wray.
- *DPLR*: Seokkwan Yoon and Almudena Parente.
- *PATO*: Joshua Monk, George Bellas and Jean Lachaud.
- *UIUC*: Marco Panesi and Francesco Panerai.
- *PMM*: Joseph Ferguson, Federico Semeraro, Krishnan Gopalan and Arnaud Borner.
- *ESM*: Aaron Brandis and Michael Barnhardt.

and more

References

[1] Meurisse, Jeremie B.E., et al. “Three-dimensional unsteady model of arc heater plasma flow”, unpublished manuscript.
[2] Fraile Izquierdo, Sergio, et al. "Analysis of Three Multi-Band Models for Radiative Heat Transfer in LTE Air Plasma." AIAA Scitech 2020 Forum. 2020.
[3] Haw, Magnus A., et al. "Preliminary Measurements of the Motion of Arcjet Current Channel Using Inductive Magnetic Probes." AIAA Scitech 2020 Forum. 2020.
[4] Ventura Diaz, Patricia, et al. "High-Fidelity Numerical Analysis of Arc-Jet Aerothermal Environments." AIAA Scitech 2020 Forum.
[5] Lachaud, Jean, et al. "A generic local thermal equilibrium model for porous reactive materials submitted to high temperatures." International Journal of Heat and Mass Transfer 108 (2017): 1406-1417.
[6] Lachaud, Jean, et al. "Porous-material analysis toolbox based on OpenFOAM and applications." Journal of Thermophysics and Heat Transfer 28.2 (2014): 191-202.
[7] Meurisse, Jeremie BE, et al. "Multidimensional material response simulations of a full-scale tiled ablative heatshield." *Aerospace Science and Technology* 76 (2018): 497-511.
[8] Thornton, John, et al. “Coupling of the Material Response and Aerothermal Environment via Pyrolysis Gas Blowing.” AIAA Scitech 2021.
[9] Torres-Herrador, Francisco, et al. "A high heating rate pyrolysis model for the Phenolic Impregnated Carbon Ablator (PICA) based on mass spectroscopy experiments." Journal of Analytical and Applied Pyrolysis 141 (2019): 104625.
[10] Meurisse, Jeremie B.E., et al. "Inverse Determination of Aeroheating and Charring Ablator Response." (2018).
[11] Thornton, John M, et al. “Determination of Aerothermal Environment and Ablator Material Response Using Inverse Methods.” (2019).
[12] Bessire, Brody K., et al. “Progress Towards Modeling The Mars Science Laboratory PICA-Nusil Heatshield.” International Planetary Probe Workshop 2019, July 2019.
[13] Bessire, Brody K., et al. “Analysis of the PICA-NuSil HyMETS Arc-Jet Campaign.” 11th Ablation Workshop, September 2019.
[14] Meurisse, Jeremie B.E., et al. "Progress towards modeling the ablation response of NuSil-coated PICA." 11th Ablation Workshop, September 2019.
[15] Ventura Diaz, Patricia, et al. “High-Fidelity Simulations of HyMETS Arc-Jet Flows for PICA-N Modeling” AIAA Scitech 2021.
[16] Meurisse, Jeremie B.E., et al. “PICA-NuSil modeling compared to HyMETS data.”, unpublished manuscript.

and more